

Effective $\bar{K}N$ interaction based on chiral SU(3) dynamics

Tetsuo Hyodo*

*Physik-Department, Technische Universität München, D-85747 Garching, Germany and
Yukawa Institute for Theoretical Physics, Kyoto University, Kyoto 606-8502, Japan*

Wolfram Weise

*Physik-Department, Technische Universität München, D-85747 Garching, Germany
(Dated: October 24, 2018)*

The effective $\bar{K}N$ interaction based on chiral SU(3) coupled-channel dynamics is derived and its extrapolation below the $\bar{K}N$ threshold is studied in detail. Starting from the coupled-channel scattering equations, we eliminate the channels other than $\bar{K}N$ and obtain an effective interaction in the single $\bar{K}N$ channel. An equivalent local potential in coordinate space is constructed such as to reproduce the full scattering amplitude of the chiral SU(3) coupled-channel framework. We discuss several realistic chiral SU(3)-based models in comparison to reach conclusions about the uncertainties involved. It turns out that, in the region relevant to the discussion of deeply bound \bar{K} -nuclear few-body systems, the resulting energy-dependent, equivalent local potential is substantially less attractive than the one suggested in previous purely phenomenological treatments.

PACS numbers: 13.75.Jz, 14.20.-c, 11.30.Rd

Keywords: Chiral SU(3) dynamics, $\Lambda(1405)$ resonance

I. INTRODUCTION

The quest for quasibound antikaon-nuclear states has become a persistently hot topic in nuclear physics. It is argued that if the $\bar{K}N$ interaction is sufficiently strong and attractive so that \bar{K} -nuclear bound systems can be formed, with binding energies so large that they fall below the $\bar{K}N \rightarrow \pi\Sigma$ threshold, such states could be narrow. An experiment performed at KEK with stopped K^- on ^4He [1] seemed to indicate such deeply bound narrow structures. However, the repetition of this experiment with better statistics [2] did not confirm the previously published results. The FINUDA measurements with stopped K^- on $^6,^7\text{Li}$ and ^{12}C targets [3] suggested an interpretation in terms of quasibound K^-pp clusters with binding energy $B(K^-pp) = (115 \pm 9)$ MeV and width $\Gamma = (67 \pm 16)$ MeV. However, this interpretation was subsequently criticized in Refs. [4, 5] with the argument that the observed spectrum may be explained by final-state interactions of the produced Λp pairs. Although these issues are unsettled, the experimental search for kaonic nuclei continues vigorously.

Calculations of strong binding of antikaons in a nuclear medium based on chiral SU(3) dynamics have a long history (see, *e.g.*, Refs. [6, 7, 8, 9, 10, 11]), starting from the early discussions of kaon condensation in dense matter [12, 13]. The recent revival of this theme was prompted by Akaishi and Yamazaki [14, 15, 16], who used a simple potential model [unconstrained by chiral SU(3)] to calculate bound states of few-body systems such as K^-pp , K^-ppn , and K^-pnn . The possibility that such systems could be highly compressed was suggested

in Ref. [15], but this was considered [17] to be an artifact of an unrealistic nucleon-nucleon interaction being used.

Faddeev calculations were performed for $\bar{K}NN$ with phenomenological input [18, 19], and with a leading-order chiral interaction [20]. Both studies found a K^-pp quasibound state above the $\pi\Sigma N$ threshold with relatively large width. The $\bar{K}NN$ system has also been studied in Ref. [21] by using a variational approach with phenomenological local potentials [14], leading to a bound state at about 50 MeV below the $\bar{K}NN$ threshold.

One should note that the predictive power of all such investigations is limited because the energy range of the $\bar{K}N$ interaction relevant for deeply bound kaonic nuclei lies far below the $\bar{K}N$ threshold. Constraints from $\bar{K}N$ scattering and from kaonic hydrogen measurements are restricted to $\sqrt{s} \geq 1432$ MeV. The only experimental information available below the $\bar{K}N$ threshold is the invariant mass spectrum in the $\pi\Sigma$ channel where the $\Lambda(1405)$ resonance is observed. However, fitting the interaction to these data involves a subtlety as we will discuss in this paper. It turns out, namely, that the peak position in the $\pi\Sigma$ mass spectrum is not to be identified with the pole position of the $\Lambda(1405)$ in the $\bar{K}N$ amplitude. Thus, naively assigning a K^-p binding energy of 27 MeV to the $\Lambda(1405)$, as is frequently done in phenomenological potential approaches, is not justified in view of the strong $\bar{K}N \leftrightarrow \pi\Sigma$ coupled-channel dynamics. In any event, we need to extrapolate the interaction calibrated around the $\bar{K}N$ threshold down to much lower energies to explore the possible existence of deeply bound \bar{K} -nuclear systems. Ambiguities in performing such extrapolations certainly arise and require a careful and detailed assessment.

A reliable and realistic starting point for a theory of low-energy $\bar{K}N$ interactions is the coupled-channel approach based on the chiral SU(3) meson-baryon effective

*Electronic address: thyodo@ph.tum.de

Lagrangian, developed and first applied in Ref. [22], and subsequently expanded by several groups [23, 24, 25]. Unitarization of the chiral interaction correctly reproduces the $\bar{K}N$ scattering observables and provides a framework for generating the $\Lambda(1405)$ resonance dynamically as a $\bar{K}N$ quasibound state embedded in the strongly interacting $\pi\Sigma$ continuum. Given that this approach is successful over a wide range of energies and a variety of channels, we would like to investigate in detail what chiral SU(3) dynamics tells us about the $\bar{K}N$ interaction below threshold.

For variational calculations of few-body systems involving antikaons, one must use a realistic effective $\bar{K}N$ interaction, preferentially in the form of a potential. This potential is generally complex and energy dependent. It must be constrained to reproduce the scattering amplitudes in vacuum, and it must encode the full coupled-channel dynamics. The first attempts in this direction, which use a schematic effective interaction, have been reported in Refs. [17, 26]. Here we would like to explicitly derive such an effective interaction in the single $\bar{K}N$ channel and construct an equivalent, energy-dependent local potential, starting from chiral SU(3) coupled-channel scattering. This interaction can then be used in \bar{K} -nuclear few-body calculations [27].

This paper is organized as follows. In Sec. II we introduce the chiral coupled-channel framework for $S = -1$ meson-baryon scattering. We present a general framework for constructing an effective interaction with reduced number of channels in a system of coupled-channel scattering equations, with full incorporation of the dynamics in the eliminated channels. In Sec. III this formalism will be applied to the $I = 0$ $\bar{K}N$ channel, showing how the $\pi\Sigma$ and other channels affect the $\bar{K}N$ single-channel interaction. We study the pole structure of the $\Lambda(1405)$ in the complex energy plane and discuss the physical origin of the singularities. We also construct the $I = 1$ effective interaction and estimate theoretical uncertainties for subthreshold extrapolations in both the $I = 0$ and $I = 1$ $\bar{K}N$ channels. Finally we derive, for practical use, an “equivalent” local potential in coordinate space in Sec. IV. A comparison is performed with amplitudes calculated from the phenomenological potential of Ref. [21], and substantial differences are pointed out. The last section presents a summary and conclusions.

II. FORMAL FRAMEWORK

A. Chiral SU(3) dynamics with coupled channels

Consider meson-baryon scattering in the strangeness $S = -1$ channel. The amplitude of coupled-channel scattering, $T_{ij}(\sqrt{s})$, taken at a total center-of-mass energy \sqrt{s} , satisfies the Bethe-Salpeter equation [22, 23, 24, 25]

$$T_{ij}(\sqrt{s}) = V_{ij}(\sqrt{s}) + V_{il}(\sqrt{s}) G_l(\sqrt{s}) T_{lj}(\sqrt{s}), \quad (1)$$

with the interaction kernel V_{ij} and the meson-baryon loop integral G_i , and channel indices i, j . This set of coupled integral equations represents the nonperturbative resummation of s -channel loop diagrams. The solution of Eq. (1) is given in matrix form by

$$T = [V^{-1} - G]^{-1},$$

under the on-shell factorization [23]. [51] This form of the amplitude is also obtained in the N/D method by neglecting the contributions from the left-hand cut [24]. This guarantees the unitarity of the scattering amplitude.

In the present work the interaction kernel V_{ij} is identified with the leading (Weinberg-Tomozawa) terms derived from the chiral SU(3) effective Lagrangian,

$$V_{ij}(\sqrt{s}) = -\frac{C_{ij}}{4f^2}(2\sqrt{s} - M_i - M_j)\sqrt{\frac{E_i + M_i}{2M_i}}\sqrt{\frac{E_j + M_j}{2M_j}}, \quad (2)$$

where f is the pseudoscalar meson decay constant, and M_i and E_i are the mass and the energy, respectively, of the baryon in channel i . A detailed study of interaction terms beyond leading order has been performed in Refs. [28, 29]. It was found that such higher order corrections are relevant for quantitative fine tuning but that the essential features of $\bar{K}N$ coupled-channel dynamics can already be reproduced at the leading-order level, the strategy that we follow here. Effects of higher order terms will be discussed in Sec. III C

The coupling strengths C_{ij} in Eq. (2) are collected in the matrix

$$C_{ij}^{I=0} = \begin{pmatrix} 3 & -\sqrt{\frac{3}{2}} & \frac{3}{\sqrt{2}} & 0 \\ & 4 & 0 & \sqrt{\frac{3}{2}} \\ & & 0 & -\frac{3}{\sqrt{2}} \\ & & & 3 \end{pmatrix},$$

for the $S = -1$ and $I = 0$ channels: $\bar{K}N$ (channel 1), $\pi\Sigma$ (channel 2), $\eta\Lambda$ (channel 3), and $K\Xi$ (channel 4). The coupling strengths in $I = 1$ channels are given by

$$C_{ij}^{I=1} = \begin{pmatrix} 1 & -1 & -\sqrt{\frac{3}{2}} & -\sqrt{\frac{3}{2}} & 0 \\ & 2 & 0 & 0 & 1 \\ & & 0 & 0 & -\sqrt{\frac{3}{2}} \\ & & & 0 & -\sqrt{\frac{3}{2}} \\ & & & & 1 \end{pmatrix},$$

for the channels $\bar{K}N$ (channel 1), $\pi\Sigma$ (channel 2), $\pi\Lambda$ (channel 3), $\eta\Sigma$ (channel 4), and $K\Xi$ (channel 5).

The loop function $G_i(\sqrt{s})$ is given by

$$G_i = i \int \frac{d^4q}{(2\pi)^4} \frac{2M_i}{[(P-q)^2 - M_i^2 + i\epsilon](q^2 - m_i^2 + i\epsilon)}.$$

Using dimensional regularization the finite parts of G_i become

$$G_i(\sqrt{s}) = \frac{2M_i}{(4\pi)^2} \left\{ a_i(\mu) + \ln \frac{M_i^2}{\mu^2} + \frac{m_i^2 - M_i^2 + s}{2s} \ln \frac{m_i^2}{M_i^2} + \frac{\bar{q}_i}{\sqrt{s}} \ln \frac{\phi_{++}(s)\phi_{+-}(s)}{\phi_{-+}(s)\phi_{--}(s)} \right\}, \quad (3)$$

with

$$\phi_{\pm\pm}(s) = \pm s \pm (M_i^2 - m_i^2) + 2\bar{q}_i\sqrt{s},$$

where $a_i(\mu)$ are subtraction constants in the channels i and μ is the renormalization scale, m_i is the mass of the meson in channel i , and $\bar{q}_i = \sqrt{[s - (M_i - m_i)^2][s - (M_i + m_i)^2]}/(2\sqrt{s})$ is the relevant momentum variable which corresponds to the meson three-momentum in the center-of-mass system above threshold.

It has been shown that the scattering amplitude constructed in this way reproduces the scattering observables, such as scattering cross sections and threshold branching ratios. The unitarized amplitude has poles in the complex energy plane at the positions of dynamically generated resonances, the properties of which are also well described [22, 23, 24, 25, 28, 29, 30, 31, 32, 33, 34, 35].

B. Single-channel effective interaction

In this section we construct an effective interaction in a given single channel, the requirement being that the resulting amplitude is identical to the solution of the full coupled-channel equations. We start with the simplest case of two-channel scattering. The aim is to incorporate the dynamics of channel 2 in an effective interaction, V^{eff} , operating in channel 1. We would like to obtain the solution T_{11} of Eq. (1) by solving a single-channel equation with kernel interaction V^{eff} , namely,

$$\begin{aligned} T^{\text{eff}} &= V^{\text{eff}} + V^{\text{eff}} G_1 T^{\text{eff}} \\ &= [(V^{\text{eff}})^{-1} - G_1]^{-1} \\ &= T_{11}. \end{aligned} \quad (4)$$

Consistency with Eq. (1) requires that V^{eff} be the sum of the bare interaction, V_{11} , in this channel and the contribution \tilde{V}_{11} from channel 2:

$$V^{\text{eff}} = V_{11} + \tilde{V}_{11}, \quad (5)$$

$$\begin{aligned} \tilde{V}_{11} &= V_{12} G_2 V_{21} + V_{12} G_2 T_{22}^{\text{single}} G_2 V_{21} \\ &= V_{12} G_2 \left[1 + T_{22}^{\text{single}} G_2 \right] V_{21}, \end{aligned} \quad (6)$$

where T_{22}^{single} is the single-channel resummation of interactions in channel 2:

$$\begin{aligned} T_{22}^{\text{single}} &= V_{22} + V_{22} G_2 T_{22}^{\text{single}} \\ &= [V_{22}^{-1} - G_2]^{-1}. \end{aligned} \quad (7)$$

Note that \tilde{V}_{11} includes iterations of one-loop terms in channel 2 to all orders. If the diagonal component V_{22} is absent, the resummation in channel 2 disappears. Therefore, this resummation term reflects the effect of the coupled-channel dynamics. Equations. (4), (5), and (7) are diagrammatically illustrated in Fig. 1.

C. Multichannel effective interaction

It is straightforward to extend this framework to the case with N channels. We can generalize Eqs. (6) and (7) to include the effect of $N - 1$ channels ($2, 3, \dots, N$) into channel 1 as

$$\tilde{V}_{11} = \sum_{m=2}^N V_{1m} G_m V_{m1} + \sum_{m,l=2}^N V_{1m} G_m T_{ml}^{(N-1)} G_l V_{l1}, \quad (8)$$

$$\begin{aligned} T_{ml}^{(N-1)} &= V_{ml}^{(N-1)} + \sum_{k=2}^N V_{mk}^{(N-1)} G_k^{(N-1)} T_{kl}^{(N-1)} \\ &= [(V^{(N-1)})^{-1} - G^{(N-1)}]^{-1}, \quad m, l = 2, 3, \dots, N. \end{aligned}$$

The last equation is given as an $(N-1) \times (N-1)$ matrix of the channels ($2, 3, \dots, N$). The amplitude of channel 1 is obtained by solving the single-channel scattering equation (4) with the effective interaction of Eqs. (5) and (8).

In general, we can reduce the N -channel problem into effective n channels ($1, 2, \dots, n$) that include the dynamics of $N - n$ channels ($n+1, n+2, \dots, N$). Starting from the full coupled-channel equation

$$T_{IJ}^{(N)} = V_{IJ}^{(N)} + \sum_{K=1}^N V_{IK}^{(N)} G_K^{(N)} T_{KJ}^{(N)} \quad (I, J \in N),$$

we want to reproduce the solution of this equation in channels ($1, 2, \dots, n$) by the effective interaction $V_{ij}^{(n)}$ as

$$\begin{aligned} T_{ij}^{(n)} &= V_{ij}^{(n)} + \sum_{k=1}^n V_{ik}^{(n)} G_k^{(n)} T_{kj}^{(n)} \quad (i, j \in n) \\ &= \left([(V^{(n)})^{-1} - G^{(n)}]^{-1} \right)_{ij} \\ &= T_{IJ}^{(N)} \quad (I, J \in n). \end{aligned}$$

The effective interaction takes the form

$$\begin{aligned} V_{ij}^{(n)} &= V_{ij} + \tilde{V}_{ij}, \\ \tilde{V}_{ij} &= \sum_{\alpha=n+1}^N V_{i\alpha} G_\alpha V_{\alpha j} + \sum_{\alpha,\beta=n+1}^N V_{i\alpha} G_\alpha T_{\alpha\beta}^{(N-n)} G_\beta V_{\beta j} \\ &\quad \alpha, \beta \in n+1, n+2, \dots, N, \end{aligned}$$

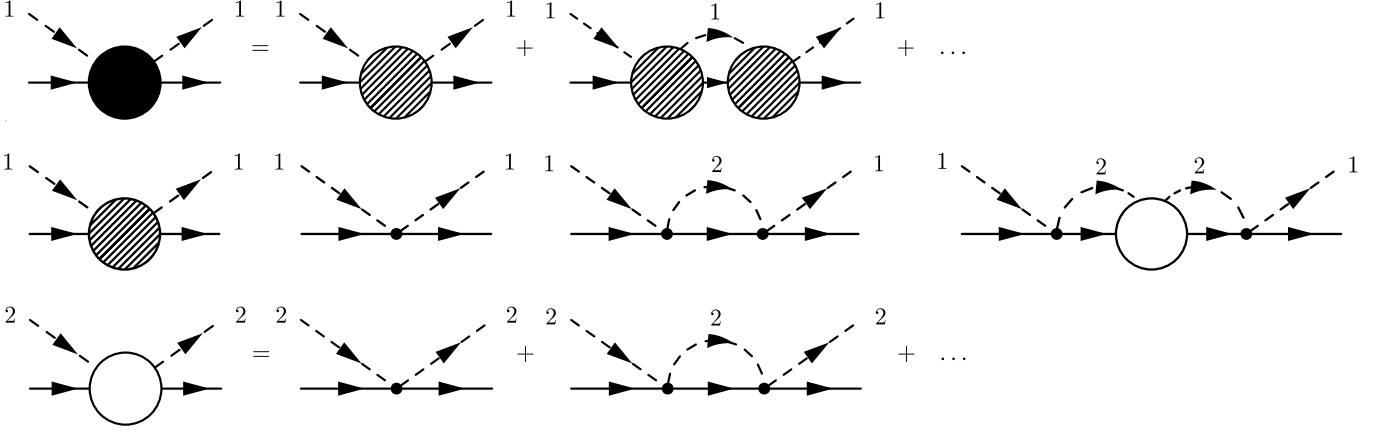


FIG. 1: Diagrammatic representation of Eqs. (4), (5), and (7). The black blob stands for $T^{\text{eff}} = T_{11}$, shaded blobs stand for V^{eff} , and white blobs denote T_{22}^{single} .

with $N - n$ channel resummation

$$\begin{aligned}
 T_{\alpha\beta}^{(N-n)} &= V_{\alpha\beta}^{(N-n)} + \sum_{\gamma=n+1}^N V_{\alpha\gamma}^{(N-n)} G_{\gamma}^{(N-n)} T_{\gamma\beta}^{(N-n)} \\
 &= \left(\left[(V^{(N-n)})^{-1} - G^{(N-n)} \right]^{-1} \right)_{\alpha\beta}, \\
 &\quad \alpha, \beta \in n+1, n+2, \dots, N
 \end{aligned}$$

III. EFFECTIVE INTERACTION

A. Analysis of the $I = 0$ $\bar{K}N$ amplitude

We now turn to our central theme, the construction of the single-channel effective $\bar{K}N$ interaction in the isospin basis. There is a strong attractive interaction in the $I = 0$ channel where the $\Lambda(1405)$ is dynamically generated. One expects that a large contribution to the $\bar{K}N$ interaction comes from the $\pi\Sigma$ channel. It is therefore useful and instructive to compare the effective interaction in the $\bar{K}N$ - $\pi\Sigma$ coupled-channel case (two-channel model) with that including four coupled channels (full model).

The parameters in Eqs. (2) and (3) are fixed as $f = 106.95$ MeV, $\mu = 630$ MeV, and $a_i = -1.96$ for all channels. We use the physical hadron masses averaged over isospin multiplets. As shown in Refs. [30, 34], the model with these parameters reproduces the experimental observables such as total cross sections for elastic and inelastic K^-p scattering, threshold branching ratios, and the $\pi\Sigma$ mass spectrum in the region of the $\Lambda(1405)$.

In what follows we present forward scattering amplitudes in units of femtometers, related to the amplitudes T in Eq. (1) by

$$F_{\bar{K}N} = -\frac{M_N}{4\pi\sqrt{s}} T_{11}, \quad F_{\pi\Sigma} = -\frac{M_\Sigma}{4\pi\sqrt{s}} T_{22},$$

etc. With this commonly used convention, scattering lengths are directly given by the values of F_i at threshold.

Let us examine separately the contributions to the effective interaction V^{eff} . The left panel of Fig. 2 shows the real and imaginary parts of the amplitude with $\pi\Sigma$ single-channel resummation [T_{22}^{single} in Eq. (7)]. At first sight there appears to be no prominent resonance structure in this amplitude, but it nevertheless develops a pole in the complex energy plane at

$$z_2(\pi\Sigma \text{ only}) = 1388 - 96i \text{ MeV}. \quad (9)$$

The large imaginary part, in spite of the relatively small phase space (~ 50 MeV above the threshold) is a special feature of this s -wave $\pi\Sigma$ single-channel resonance.

In the right panel of Fig. 2, the $\bar{K}N$ interaction \tilde{V}_{11} from coupled-channel dynamics [Eqs. (6) and (8)] are plotted. Thin lines represent the results with the two-channel model; the results of the full model are also shown as thick lines.

One also observes that the imaginary part of \tilde{V}_{11} is almost identical in the two-channel and full models. The reason is as follows. First, the imaginary part of \tilde{V}_{11} comes only from the loop of the $\pi\Sigma$ channel G_2 in this energy region, when we expand the amplitude. Taking into account the zeros in the coupling strengths $C_{23} = C_{32} = C_{14} = C_{41} = 0$, one can show that the difference between $\text{Im}\tilde{V}_{11}^{(2)}$ and $\text{Im}\tilde{V}_{11}^{(4)}$ is of the order of $\mathcal{O}[V(GV)^3]$. However, the magnitude of GV is roughly estimated as $\mathcal{O}(10^{-1})$. Numerically, the magnitudes of the real and imaginary parts are smaller than 0.7 for the relevant energy region. Therefore, terms with $\mathcal{O}[V(GV)^3]$ are much smaller in magnitude than the imaginary part of \tilde{V}_{11} , which is of order $\mathcal{O}[V(GV)]$. Hence the difference between $\text{Im}\tilde{V}_{11}^{(4)}$ and $\text{Im}\tilde{V}_{11}^{(2)}$ is indeed small.

The effective $\bar{K}N$ interaction V^{eff} is plotted in Fig. 3, together with the tree-level Weinberg-Tomozawa term for the $\bar{K}N$ channel. By construction of the effective interaction [Eq. (5)], the difference from the tree-level one is

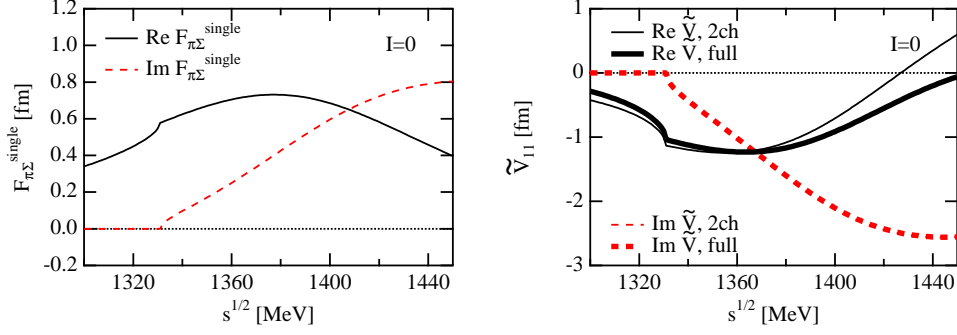


FIG. 2: (Color online) The single-channel $\pi\Sigma$ scattering amplitude $F_{\pi\Sigma}^{\text{single}} = -(4\pi M_\Sigma/\sqrt{s}) T_{22}^{\text{single}}$ (left panel) and the interaction term \tilde{V}_{11} (right panel). Real parts are shown as solid lines; imaginary parts are represented as dashed lines. The thin lines are the result of the two-channel model and the thick lines are the result of the full (four-channel) model. The imaginary parts of \tilde{V}_{11} in the two-channel and full models are indistinguishable in this figure.

attributed to the coupled-channel dynamics. As seen in the figure, the $\pi\Sigma$ and other coupled channels enhance the strength of the interaction at low energy, although not by a large amount. The primary difference is seen in the energy dependence of the interaction kernel. The imaginary part is smaller in magnitude than the real part. This permits treating the imaginary part perturbatively in the effective $\bar{K}N$ interaction.

In the left panel of Fig. 4, we show the result of $\bar{K}N$ scattering amplitude T^{eff} , obtained by solving the single-channel scattering equation with V^{eff} . The full amplitude in the $\pi\Sigma$ channel is plotted in the right panel for comparison. We numerically checked that T^{eff} coincides with T_{11} resulting from the coupled-channel equations.

In the $\bar{K}N$ scattering amplitude, the resonance structure is observed at around 1420 MeV, significantly higher than the nominal position of the $\Lambda(1405)$. However, the peak in the $\pi\Sigma$ amplitude (shown in the right panel of Fig. 4) is in fact located close to 1405 MeV. This is a consequence of the two-pole structure [36, 37, 38], which we will discuss in detail in the following sections. Results with the full model (thick lines) are not very much different from those with the two-channel model (thin lines). This indicates that the scattering amplitude around the $\bar{K}N$ threshold is well described by the $\bar{K}N$ - $\pi\Sigma$ coupled-channel system, and we confirm that the $\eta\Lambda$ and $K\Xi$ channels are unimportant for the physics of the $\bar{K}N$ interaction in the energy region of interest.

B. Structure of $\Lambda(1405)$

We now discuss the pole structure of the $\Lambda(1405)$ resonance in greater detail. The $\bar{K}N$ scattering amplitude $T^{\text{eff}}(\sqrt{s})$, obtained by using the two-channel model, develops two poles at

$$z_1^{(2)} = 1432 - 17i \text{ MeV}, \quad z_2^{(2)} = 1398 - 73i \text{ MeV}.$$

These pole positions move slightly, to

$$z_1^{(4)} = 1428 - 17i \text{ MeV}, \quad z_2^{(4)} = 1400 - 76i \text{ MeV},$$

in the full model with four channels. Again, the deviation from the two-channel model is only marginal. We thus confirm the dominance of the $\bar{K}N$ - $\pi\Sigma$ coupled-channel dynamics in the $\bar{K}N$ amplitude. As discussed in Ref. [36], the poles z_1 and z_2 have different coupling strengths to the $\pi\Sigma$ and $\bar{K}N$ channels, leading to the different shapes in the $\bar{K}N$ and $\pi\Sigma$ amplitudes, as seen in Fig. 4.

Next we study the origin of these poles. As previously mentioned, there is a pole [Eq. (9)] in the amplitude T_{22} representing $\pi\Sigma$ single-channel resummation. We can also perform the resummation of the tree-level Weinberg-Tomozawa term in the single $\bar{K}N$ channel, which generates a bound state pole at

$$z_1(\bar{K}N \text{ only}) = 1427 \text{ MeV}.$$

The pole positions for single-channel, two-channel, and full models are plotted in Fig. 5. These positions obviously suggest that the pole $z_1(\bar{K}N \text{ only})$ is the origin of the poles $z_1^{(2)}$ and $z_1^{(4)}$, whereas $z_2(\pi\Sigma \text{ only})$ is the origin of the poles $z_2^{(2)}$ and $z_2^{(4)}$. This observation agrees once again with the qualitative behavior discussed in Refs. [36, 39] that the pole z_1 strongly couples to the $\bar{K}N$ channel and the pole z_2 to the $\pi\Sigma$ channel.

The principal features from chiral SU(3) dynamics underlying this behavior are as follows. The driving (attractive) s -wave interactions in the $\bar{K}N$ and $\pi\Sigma$ channels are determined by the Goldstone boson nature of the pseudoscalar octet mesons. In the chiral limit (i.e., with all quark masses $m_{u,d}$ and m_s strictly equal to zero) these interactions would all vanish at threshold, with massless kaon and pion. Chiral symmetry dictates that their interaction strength grows linearly (in leading order) with their energy. Explicit chiral symmetry breaking gives those mesons their masses and moves the meson-baryon threshold energies to their physical values. At

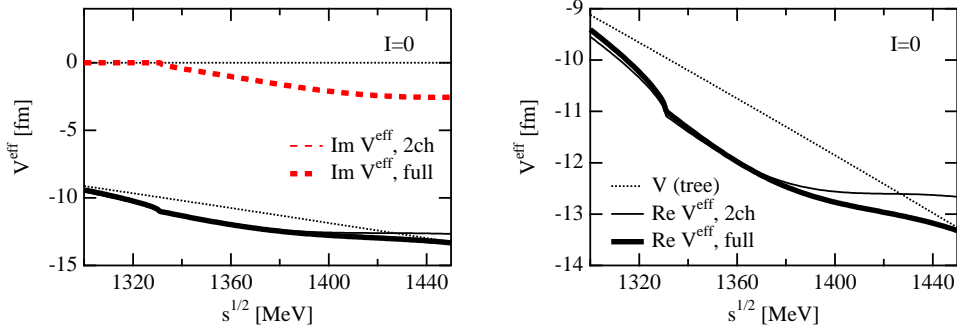


FIG. 3: (Color online) The $\bar{K}N$ ($I = 0$) interaction at tree level given by the Weinberg-Tomozawa term (dotted lines), the effective interaction in the two-channel model (thin lines), and the effective interaction in the full model (thick lines). The real parts are shown by the solid lines, and the imaginary parts are depicted by the dashed lines. The right panel details the upper part of the left panel. The imaginary parts of V^{eff} in the two-channel and full models are indistinguishable in this figure.

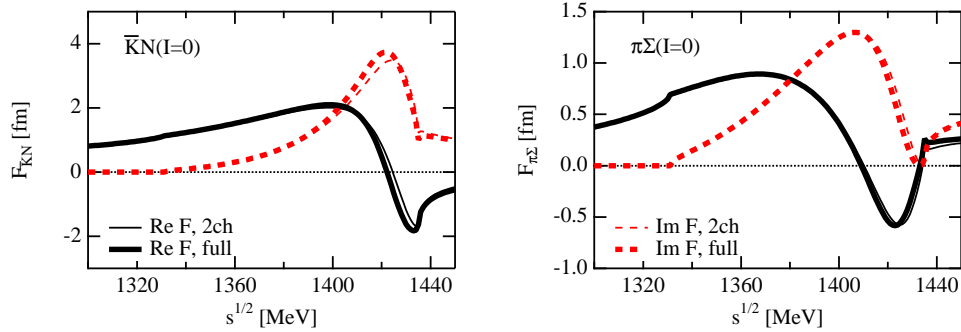


FIG. 4: (Color online) Scattering amplitudes $F_{\bar{K}N}$ channel (left) and $F_{\pi\Sigma}$ (right) in the ($I = 0$) two-channel model (thin lines) and in the full model (thick lines). Real parts are shown as solid lines and imaginary parts as dashed lines.

the kaon-nucleon threshold, the leading $\bar{K}N$ interaction, $V_{11} \sim -\frac{3m_K}{2f^2}$, becomes sufficiently attractive to produce a weakly bound state. At the $\pi\Sigma$ threshold the corresponding leading $\pi\Sigma$ interaction, $V_{22} \sim -\frac{2m_\pi}{f^2}$, is too weak to support a $\pi\Sigma$ bound state, but it still generates a resonance above threshold.

At a more quantitative level, the driving attractive (Weinberg-Tomozawa) interaction terms in the $S = -1$ meson-baryon channels, with their characteristic energy dependence,

$$V_{11} \equiv V_{\bar{K}N} \simeq -\frac{3}{2f^2} (\sqrt{s} - M_N)$$

and

$$V_{22} \equiv V_{\pi\Sigma} \simeq -\frac{2}{f^2} (\sqrt{s} - M_\Sigma),$$

generate a $\bar{K}N$ bound state and a $\pi\Sigma$ resonance already in the absence of channel couplings (i.e., for $V_{12} = V_{21} = 0$). In the typical energy range of $\sqrt{s} \sim 1410$ – 1420 MeV of interest here, the ratio of these driving interactions,

$$\frac{V_{\bar{K}N}}{V_{\pi\Sigma}} \sim -\frac{3}{4} \left(\frac{\sqrt{s} - M_N}{\sqrt{s} - M_\Sigma} \right)$$

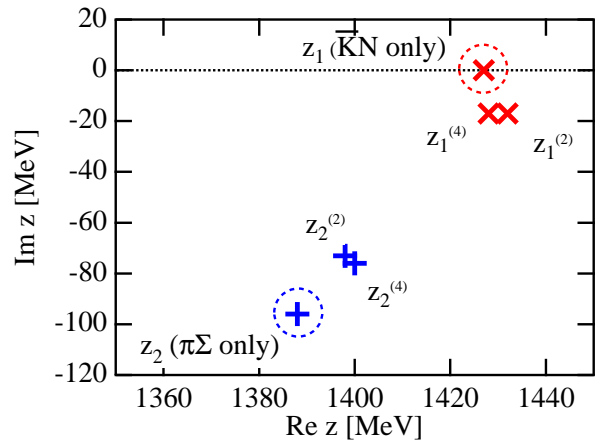


FIG. 5: (Color online) Pole positions of the $\bar{K}N(I = 0)$ scattering amplitude resulting from the single-channel, two-channel, and full (four-channel) models.

is about 1.6. The $\bar{K}N$ interaction is effectively stronger, but the $\pi\Sigma$ interaction is sizable and cannot be ignored even though the $\pi\Sigma$ resonance pole is located at a consid-

erable distance from the real axis in the complex energy plane. The isolated $\bar{K}N$ bound state, in contrast, has a binding energy of only 5 MeV at this stage. By turning on the nondiagonal $\bar{K}N \leftrightarrow \pi\Sigma$ couplings, $V_{12} = V_{21}$, both the $\pi\Sigma$ resonance and $\bar{K}N$ bound state poles move to their final positions as shown in Fig. 5. The $\bar{K}N$ bound state turns into a quasibound state embedded in the $\pi\Sigma$ continuum, with a decay width of about 35 MeV. At the same time, by its coupling to the (virtual) $\bar{K}N$ channel, the previously isolated $\pi\Sigma$ resonance shifts and reduces its width by about 20%, from $\Gamma_{\pi\Sigma} \simeq 190$ MeV to $\Gamma_{\pi\Sigma} \simeq 150$ MeV.

These considerations imply a subtlety in assigning a mass (or a $\bar{K}N$ binding energy) to the $\Lambda(1405)$. Empirically, the only information at hand is the $\pi\Sigma$ mass spectrum given by the imaginary part of $T_{22} \equiv T_{\pi\Sigma}$ [see Fig. 4 (right)]. This mass spectrum has its maximum indeed at $\sqrt{s} \simeq 1405$ MeV. Although its spectral shape is far from that of a Breit-Wigner resonance form, one may nevertheless read off a width of about 50 MeV. This is the mass and width assignment given to the $\Lambda(1405)$ in the Particle Data Group table. However, the amplitude $T^{\text{eff}} = T_{11} \equiv T_{\bar{K}N}$ in the $\bar{K}N$ channel shown in Fig. 4 (left) in the form of $F_{\bar{K}N}$ has evidently quite different features. This is the amplitude relevant for subthreshold extrapolations of the $\bar{K}N$ interaction. The $\bar{K}N$ quasibound state, signaled by the zero of $\text{Re } F_{\bar{K}N}$, is seen to be located at $\sqrt{s} \simeq 1420$ MeV, *not* at 1405 MeV, and almost coincides with the maximum of $\text{Im } F_{\bar{K}N}$. The actual $\bar{K}N \rightarrow \pi\Sigma$ decay width is about 20% smaller than the one naively identified with the breadth of the $\pi\Sigma$ mass spectrum. One must therefore conclude that the $\bar{K}N$ quasibound state, commonly associated with the $\Lambda(1405)$, has a binding energy of only about 12 MeV (and *not* the 27 MeV often used to tune phenomenological $\bar{K}N$ potentials). [52]

Given the obvious relevance of this discussion to the existence (or nonexistence) of deeply bound \bar{K} -nuclear states, it is now important to estimate theoretical uncertainties and examine possible ambiguities.

C. Theoretical uncertainties and $I = 1$ amplitude

Detailed investigations have been performed concerning the position of the second pole z_2 , especially its sensitivity to higher order terms in the chiral effective Lagrangian [28, 29, 31, 32, 33]. This section presents a conservative assessment of such uncertainties, examining different chiral coupled-channel calculations in comparison.

Several variants of the chiral unitary approach will be used in this test, all of which start from a leading Weinberg-Tomozawa (WT) term in the interaction kernel but differ in their detailed treatment of subtraction constants. The differences among these models have their origin in the fitting procedures to experimental data, primarily through ambiguities of the $\pi\Sigma$ mass spectrum

with its limited data quality.

Oset-Ramos-Bennhold (ORB) [35] determine the subtraction constants by matching the loop function with that obtained in the three-momentum cutoff, with which they successfully reproduce the observables [23]. Hyodo-Nam-Jido-Hosaka (HNJH) [34] used one single subtraction constant in all channels to fit the data. A systematic χ^2 fit was performed by Borasoy-Niñler-Weise (BNW) [29] and by Borasoy-Meißner-Niñler [33], where all the subtraction constants were used to fit the experimental data and the influence of higher order terms in the chiral effective Lagrangian has been studied. The fitted observables in these investigations are total cross sections of K^-p scattering in elastic and inelastic channels, threshold branching ratios, invariant mass distribution in the $\pi\Sigma$ channel and the K^-p scattering length deduced from kaonic hydrogen data. The analysis in the preceding sections is based on the simpler HNJH model.

To estimate systematic theoretical uncertainties, we adopt all these models and derive the corresponding effective interactions. The definition of the subtraction constant a^{Borasoy} in Refs. [29, 33] is related to the present convention (and those in Refs. [34, 35]) by

$$a(\mu) = 16\pi^2 a^{\text{Borasoy}}(\mu) - 1.$$

Changes of the renormalization scale in different models are related by

$$a(\mu') = a(\mu) + 2 \ln(\mu'/\mu),$$

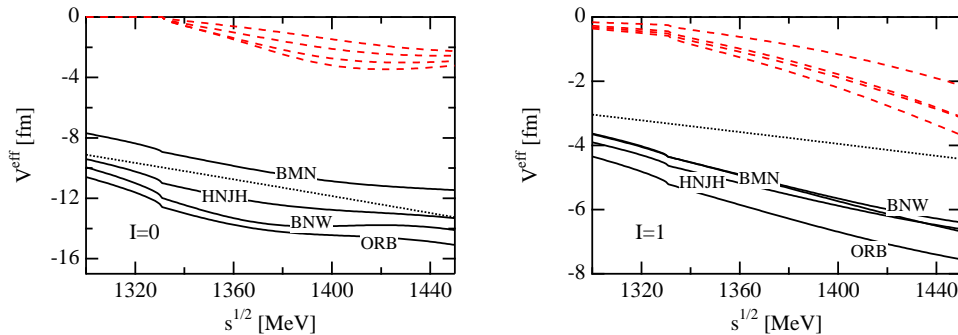
where $\mu = 630$ MeV. The subtraction constants determined in the models under consideration are shown in Table I together with the corresponding values for the meson decay constant f . [53] We use isospin-averaged hadron masses as input. One should note that the results presented here are not exactly identical to those in the original papers because of differences in the input masses, isospin breaking effects, and so on. The accuracy of the analysis is nonetheless sufficient for the present purpose of estimating theoretical uncertainties.

The effective interactions calculated with these models are shown in Fig. 6 together with the tree-level WT term result (with $f \simeq 107$ MeV, a value intermediate between the empirical pion and kaon decay constants). The strengths of the effective interactions are roughly comparable with the WT term for the $\bar{K}N(I = 0)$ channel, whereas the coupled-channel dynamics in the $\bar{K}N(I = 1)$ channel enhances the interaction strengths by about 50% from that of the WT term.

With these effective interactions we find the scattering amplitudes shown in Fig. 7. The model dependence of these amplitudes is not large despite the differences among the underlying effective interactions. This is understandable because these interactions are all fitted to similar data sets. The differences in the interaction strengths among different models are in large part compensated by corresponding differences in the subtraction constants. Note that the peak position of the imaginary

TABLE I: Subtraction constants a_i at $\mu = 630$ MeV and meson decay constant f in different models.

Reference	f (MeV)	$a_{\bar{K}N}$	$a_{\pi\Sigma}$	$a_{\eta\Lambda}$	$a_{K\Xi}$	$a_{\pi\Lambda}$	$a_{\eta\Sigma}$
ORB [35]	103.7652	-1.84	-2.00	-2.25	-2.67	-1.83	-2.38
HNJH [34]	106.95	-1.96	-1.96	-1.96	-1.96	-1.96	-1.96
BNW [29]	111.2	-1.86	-2.35	-2.67	-2.62	-1.23	-2.80
BMN [33]	120.9	-2.21	-2.38	-2.19	9.59	-3.88	-2.15

FIG. 6: (Color online) The effective interaction V^{eff} of the $\bar{K}N(I=0)$ channel (left) and that of the $\bar{K}N(I=1)$ channel (right) in different models. The real parts are shown as solid lines and imaginary parts as dashed lines. The lines correspond to the models as indicated in the figure. The dotted line is the tree-level WT interaction.TABLE II: K^-p scattering lengths and pole positions in different models.

Reference	a_{K^-p} (fm)	z_1 (MeV)	z_2 (MeV)
ORB [35]	$-0.617 + 0.861i$	$1427 - 17i$	$1389 - 64i$
HNJH [34]	$-0.608 + 0.835i$	$1428 - 17i$	$1400 - 76i$
BNW [29]	$-0.532 + 0.833i$	$1434 - 18i$	$1388 - 49i$
BMN [33]	$-0.410 + 0.824i$	$1421 - 20i$	$1440 - 76i$

part of the $\bar{K}N(I=0)$ amplitude is around 1420 MeV in all models. This observation is also consistent with the solution of the Lippmann-Schwinger equation obtained by using a chiral interaction approximated by a separable potential [20, 22].

Calculated K^-p scattering lengths $a_{K^-p} = (a_{\bar{K}N(I=0)} + a_{\bar{K}N(I=1)})/2$ and pole positions of the scattering amplitudes are summarized in Table II. The pole positions are also plotted in Fig. 8. The pole z_2 in BMN [33] is found above the $\bar{K}N$ threshold. It is located on the Riemann sheet, which is unphysical for $\pi\Sigma$ and physical for $\bar{K}N$. For $\text{Im}z < 0$ this sort of pole does not directly influence the physical scattering amplitudes.

The pole positions of z_2 are scattered over a wide range of the complex energy plane depending on the model used. Moreover, the detailed behavior of this pole is sensitive to physics beyond leading (WT) order in the chiral effective Lagrangian, studied systematically in Ref. [29]. However, such higher order corrections can partially be absorbed by readjusting the pseudoscalar decay constant f .

In contrast to the strong model dependence of z_2 the

location of the pole z_1 is quite stable, with $\text{Re } z_1$ positioned in a narrow window around 1420–1430 MeV. In spite of the differences in the position of the pole z_2 , the $\bar{K}N(I=0)$ amplitudes in Fig. 7 do not change very much. This is because the behavior of the $\bar{K}N$ amplitude is largely determined by the contribution from the pole z_1 .

The spread in the z_2 pole positions can be observed in the $\pi\Sigma$ amplitude. In Fig. 9 we plot the imaginary part of the $\pi\Sigma(I=0)$ amplitude where the maximum of the spectrum is commonly identified with the $\Lambda(1405)$ resonance. The model dependence of the $\pi\Sigma$ amplitudes is stronger than that of the $\bar{K}N$ amplitude, reflecting the contribution from the pole z_2 . For comparison, we plot the invariant mass spectrum of $\pi^-\Sigma^+$ in Ref. [40] and the sum of $\pi^\pm\Sigma^\mp$ in Ref. [41].

One should be careful when comparing the calculated $I=0$ $\pi\Sigma$ mass spectrum with experimental data. In principle we need all three $\pi\Sigma$ states ($\pi^\pm\Sigma^\mp$, $\pi^0\Sigma^0$) *simultaneously* to construct the pure $I=0$ spectrum, since there are three isospin states: $I=0, 1$, and 2 . [54] The available experimental $\pi\Sigma$ spectra were generated in one or two final states for each experiment (sum of charged states [41], $\pi^-\Sigma^+$ [40], and charged states [42], $\pi^0\Sigma^0$ [43], $\pi^0\Sigma^0$ [44]). This means in fact that the $\pi\Sigma$ mass spectrum representing the $I=0$ channel has not been extracted so far. The value quoted by the Particle Data Group (PDG) [45] is based only on the analysis of Ref. [46] in which the $\pi^-\Sigma^+$ spectrum of Ref. [40] was fitted by the $I=0$ amplitudes of theoretical models. Even if the $I=1$ and $I=2$ components are smaller than the $I=0$ spectrum, cross terms such as $\text{Re}T^0T^{1*}$ may

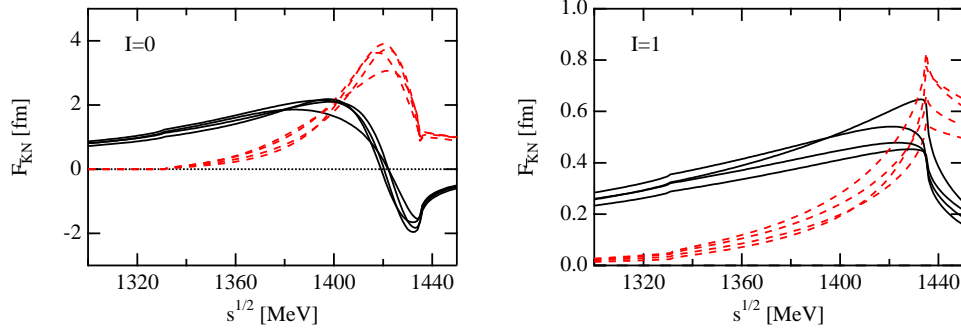


FIG. 7: (Color online) Scattering amplitude $F_{\bar{K}N} = -(4\pi M_N/\sqrt{s})T^{\text{eff}}$ of the $\bar{K}N(I=0)$ channel (left) and of the $\bar{K}N(I=1)$ channel (right) in different models. The real parts are shown as solid lines and imaginary parts as dashed lines.

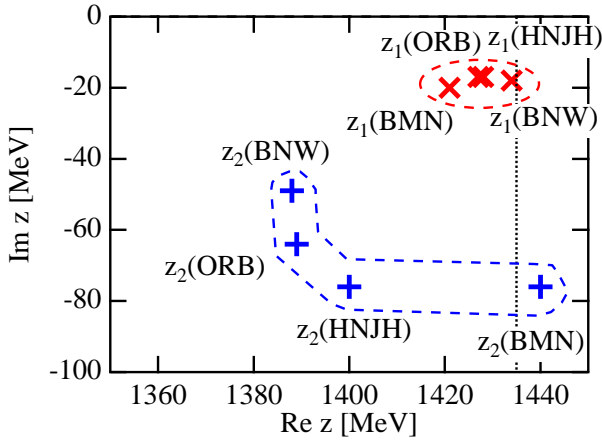


FIG. 8: (Color online) Pole positions of the $\bar{K}N(I=0)$ scattering amplitude in different models. The dotted line denotes the threshold of the $\bar{K}N$ channel.

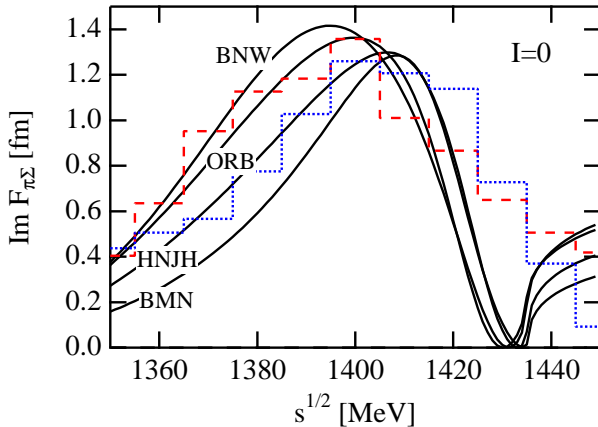


FIG. 9: (Color online) Imaginary part of the $\pi\Sigma(I=0)$ amplitude in different models. The dashed histogram indicates data from Ref. [41] ($\pi^-\Sigma^+$ spectrum) and the dotted histogram indicates data from Ref. [40] (sum of $\pi^\pm\Sigma^\mp$ spectra).

TABLE III: The real parts of the amplitude $F_{\bar{K}N}(I=0)$ at $\sqrt{s} = 1360$ MeV in comparison with the next-to-leading-order results.

Model	Re $F_{\bar{K}N}(I=0)$ (fm)	Order
this work	1.6 ± 0.2	leading
Ref. [29] WT	~ 1.6	leading
Ref. [29] c	~ 1.9	p^2
Ref. [29] s	~ 2.0	p^2

distort the shape of the spectrum [47, 48].

Additional theoretical uncertainties concern the chiral coupled-channel approach itself. The present investigation is focused on chiral SU(3) models with leading-order interaction. Effects of higher order $\bar{K}N$ couplings have been studied systematically in Ref. [29]. Representative examples are listed in Table III, which shows the values of $\text{Re } F_{\bar{K}N}(I=0)$ at a given subthreshold energy, $\sqrt{s} = 1360$ MeV. The case WT is equivalent to the leading-order results discussed in this paper. Cases c and s include next-to-leading-order terms in the chiral SU(3) interaction kernel. In all cases the input parameters are adjusted to reproduce the available experimental data. The results with inclusion of higher order terms tend to increase slightly the strength of the $\bar{K}N$ amplitude in the far-subthreshold region, within a limited uncertainty bound of about 20 %.

Early coupled-channel calculations [22, 49] suggested larger subthreshold values of $\text{Re } F_{\bar{K}N}$ (e.g., ~ 3.8 fm [22] and ~ 3.0 fm [49] at $\sqrt{s} = 1360$ MeV). These differences in comparison with the more recent chiral coupled-channel results can presumably be traced to the use of the (non-relativistic) Lippmann-Schwinger equation in combination with separable approximations and corresponding cutoffs for the interaction kernels in the early approaches, as opposed to the Bethe-Salpeter equation and dispersion relation techniques applied in the more recent computations. A common feature of all approaches is the location of the zero of $\text{Re } F_{\bar{K}N}$ above the canonical 1405 MeV, irrespective of the detailed extrapolation of the amplitude to the far-subthreshold region.

Further improvements should incorporate rigorous theoretical constraints on the subthreshold $\bar{K}N$ amplitude, such as crossing symmetry [50], as discussed within the framework of a chiral coupled-channel approach in Ref. [25]. In addition, a detailed consistency analysis of subtraction constants in view of constraints from order p^3 counter terms, as elaborated in Ref. [25], is certainly desirable along the same line as the present investigation.

Although the primary uncertainty of any detailed $\bar{K}N$ subthreshold extrapolation is evidently rooted in the lack of sufficiently accurate data for the $\pi\Sigma$ spectral functions, it is nevertheless remarkable that most chiral models consistently agree within limited errors on the shapes and magnitudes of real and imaginary parts of the $\bar{K}N$ amplitudes, in both $I = 0$ and $I = 1$ channels. The following intermediate conclusions can therefore be drawn:

- The position of the $\Lambda(1405)$ as an $I = 0$ quasibound $\bar{K}N$ state embedded in the $\pi\Sigma$ continuum, when identified with the zero of $\text{Re } T^{\text{eff}}(\bar{K}N)$, is located at $\sqrt{s} \simeq 1420$ MeV, *not* at 1405 MeV. The corresponding K^-p “binding energy” is thus 12 MeV instead of 27 MeV.
- The $\pi\Sigma$ mass spectrum (with so far very limited accuracy of the existing data base) reflects primarily coupled-channel dynamics around the z_2 pole in the $\pi\Sigma$ amplitude. The maximum of the $\pi\Sigma$ mass spectrum around $\sqrt{s} \sim (1400\text{--}1410)$ MeV is therefore *not* to be directly interpreted as the position of the $\Lambda(1405)$.

IV. “EQUIVALENT” LOCAL POTENTIAL

A. Local pseudopotential from the effective $\bar{K}N$ interaction

Next we construct an equivalent local $\bar{K}N$ pseudopotential in coordinate space. Such a potential is, for example, a useful input to computations of \bar{K} -nuclear few-body systems. Equivalence means that the solution of the Schrödinger or Lippmann-Schwinger equation with this pseudopotential should approximate the scattering amplitude derived from the full chiral coupled-channel calculation as closely as possible.

Consider an s -wave antikaon-nucleon system in nonrelativistic quantum mechanics. The Schrödinger equation for the radial wave function $u(r)$ is (with \hbar set to 1)

$$-\frac{1}{2\mu} \frac{d^2 u(r)}{dr^2} + U(r, E) u(r) = E u(r). \quad (10)$$

The potential $U(r, E)$ is complex and energy dependent. The reduced mass is given by $\mu = M_N m_K / (M_N + m_K)$. By starting from the effective interaction $V^{\text{eff}}(\sqrt{s})$ of Eq. (5), the ansatz for an equivalent local pseudopotential is

$$U(r, E) = \frac{g(r)}{2\tilde{\omega}} \frac{M_N}{\sqrt{s}} V^{\text{eff}}(\sqrt{s}), \quad (11)$$

with a form factor $g(r)$ representing the finite range of the interaction. The reduced energy $\tilde{\omega}$ is given by

$$\tilde{\omega}(\sqrt{s}) = \frac{\omega_K E_N}{\omega_K + E_N},$$

with

$$E_N = \frac{s - m_K^2 + M_N^2}{2\sqrt{s}}, \quad \omega_K = \frac{s - M_N^2 + m_K^2}{2\sqrt{s}}.$$

The energy E appearing in the Schrödinger equation (10) is related to the total c.m. energy of the two-body system by

$$E = \sqrt{s} - M_N - m_K.$$

For orientation, consider the zero-range $I = 0$ $\bar{K}N$ pseudopotential generated by the leading Weinberg-Tomozawa term in the heavy-baryon limit ($M_N \rightarrow \infty$); inserting $V^{\text{eff}} = V_{11}$ in Eq. (11) one has

$$U_{\text{WT}}^{I=0}(r) = -\frac{3}{4f^2} \delta^3(\vec{r}).$$

With $f \simeq 0.1$ GeV, the volume integral of this potential is $\int d^3r U_{\text{WT}} \simeq -0.58$ GeV.

The coupled-channel dynamics encoded in \tilde{V}_{11} of Eq. (5) involves finite range effects through the $\pi\Sigma$ loops, which are given a minimal parametrization in terms of the form factor $g(r)$. We choose a Gaussian ansatz

$$g(r) = \frac{1}{\pi^{3/2} b^3} e^{-r^2/b^2},$$

with the range parameter b . This range parameter should reflect the subtraction constant $a_{\bar{K}N}$ used in the chiral coupled-channel approach.

B. Comparison of scattering amplitudes

The $\bar{K}N$ scattering amplitude $F_{\bar{K}N}$ derived from the potential $U(r, E)$ is now calculated in the usual way. The s -wave scattering amplitude is

$$F_{\bar{K}N} = \frac{1}{k(\cot \delta_0 - i)},$$

where the phase shift δ_0 is determined by the asymptotic wave function,

$$\frac{u(r)}{r} \rightarrow A_0 [\cos \delta_0 j_0(kr) - \sin \delta_0 n_0(kr)] \quad \text{for } r \rightarrow \infty,$$

with spherical Bessel and Neumann functions j_0 and n_0 . The wave number $k = \sqrt{2\mu E}$ becomes imaginary below threshold, $E < 0$.

Given $V^{\text{eff}}(\sqrt{s})$ as input, the range parameter b is then fixed by requiring that the real part of the $\bar{K}N$ amplitude develops its zero at $\sqrt{s} \simeq 1420$ MeV to satisfy the condition for the quasibound $\bar{K}N$ state at this point. For

the HNJH model, this condition determines $b = 0.47$ fm. Note that this scale is somewhat smaller than the typical range associated with vector meson exchange, the picture that one has in mind as underlying the vector current interaction generating the Weinberg-Tomozawa term.

With $b = 0.47$ fm fixed, the $I = 0$ and $I = 1$ amplitudes generated by the equivalent local pseudopotential $U(r, E)$ reproduce the full $\bar{K}N$ coupled-channel amplitudes perfectly well in the threshold and subthreshold region above $\sqrt{s} \simeq 1420$ MeV. However, at energies below the quasibound state, the local ansatz [Eq. (11)] does not extrapolate correctly into the far-subthreshold region. One has to keep in mind that the complex, off-shell effective $\bar{K}N$ interaction is in general nonlocal and energy dependent to start with. Its detailed behavior over a broader energy range cannot be approximated by a simple local potential without paying the price of extra energy dependence. This is demonstrated in Fig. 10. In the subthreshold region below $\sqrt{s} < 1400$ MeV, the amplitudes calculated with the local potential overestimate the ones resulting from the coupled-channel approach significantly, in both $I = 0$ and $I = 1$ channels. One observes that subthreshold extrapolations using a naive local potential tend to give much stronger $\bar{K}N$ attraction than what chiral coupled-channel dynamics actually predicts. Corrections to the energy dependence of the local potential need to be applied to repair this deficiency.

C. Improved local potentials and uncertainty analysis

The necessary corrections just mentioned can easily be implemented by introducing a third-order polynomial in \sqrt{s} ,

$$U(r=0, E) = K_0 + K_1\sqrt{s} + K_2(\sqrt{s})^2 + K_3(\sqrt{s})^3, \\ 1300 \leq \sqrt{s} \leq 1450 \text{ MeV},$$

to reproduce the full coupled-channel result for $F_{\bar{K}N}$ at $\sqrt{s} < 1400$ MeV. The coefficients K_i are summarized in Tables V and VI (rows of the HNJH model). The strength of the fitted potential at $r = 0$ is shown in the upper panel of Fig. 11 by thick lines. The strength of the potential in its original form [Eq. (11)] is also shown by the dotted lines.

The resulting scattering amplitudes are presented in the lower panel of Fig. 11 together with the amplitudes resulting from the chiral unitary approach. As seen in the figure, a 20% reduction of the local potential is required to match the amplitudes in the energy region $\sqrt{s} < 1400$ MeV. As a consequence the energy dependence of the local potential becomes stronger. The matching of the amplitude in the energy range around the quasibound state and close to threshold remains unchanged, keeping the range parameter b at its previously determined value. With its improved energy dependence, the overall matching of the “equivalent” local $\bar{K}N$ potential is now quite

TABLE IV: Range parameters b of the local potential and the subtraction constants $a_{\bar{K}N}$ used in the chiral unitary approach.

Reference	b (fm)	$a_{\bar{K}N}$
ORB [35]	0.52	-1.84
HNJH [34]	0.47	-1.96
BNW [29]	0.51	-1.86
BMN [33]	0.41	-2.21

satisfactory, but the attraction in the far-subthreshold region is substantially weaker than naively anticipated.

To estimate again possible uncertainties, we apply the corrections to the energy dependence of the potentials obtained with all four variants of the chiral models studied in Sec. III C. The range parameters are determined so as to reproduce the position of the quasibound $\bar{K}N$ state at the same energy $\sqrt{s} \simeq 1420$ MeV as found with the coupled-channel amplitudes. The resulting values of the range parameter b are summarized in Table IV. The expected reciprocal relationship between subtraction constants $a_{\bar{K}N}$ and Gaussian range parameters is evident.

In all cases studied, the local potential produces scattering amplitudes that are systematically too large (i.e., too strongly attractive) at the lower energy side, when compared with the amplitudes of the chiral coupled-channel approach. Repeating the procedures as before, we improve the potentials, correcting the far-subthreshold energy dependence by matching the scattering amplitudes to the chiral coupled-channel results. These corrections are again performed by adjusting the third-order polynomial [Eq. (IV C)] in each case. The coefficients of the polynomial fit are collected in Tables V and VI.

The comparison between uncorrected and corrected potential strengths at the origin, $U(r=0, E)$, is shown in Figs. 12 and 13. The resulting scattering amplitudes are presented in Fig. 14. Note that all the potentials pictured in the right-hand panels of Figs. 12 and 13 are “equivalent” in that they reproduce the same scattering amplitudes both on- and off-shell (below threshold) to good approximation. The differences in the potential strengths at $r = 0$ are largely balanced by differences in the range parameters b , such that the volume integrals $\int d^3r U$ are in a reduced band (illustrated by the smaller spread of V^{eff} in Fig. 6) for all different versions of the chiral effective $\bar{K}N$ interactions.

D. Comparison with the phenomenological AY potential

Finally, let us compare our results with the phenomenological Akaishi-Yamazaki (AY) potential [14, 21]. This potential was introduced on purely phenomenological grounds by fitting the $\bar{K}N$ scattering data and the PDG value of the $\Lambda(1405)$ resonance. In $\bar{K}N$ - $\pi\Sigma$ coupled

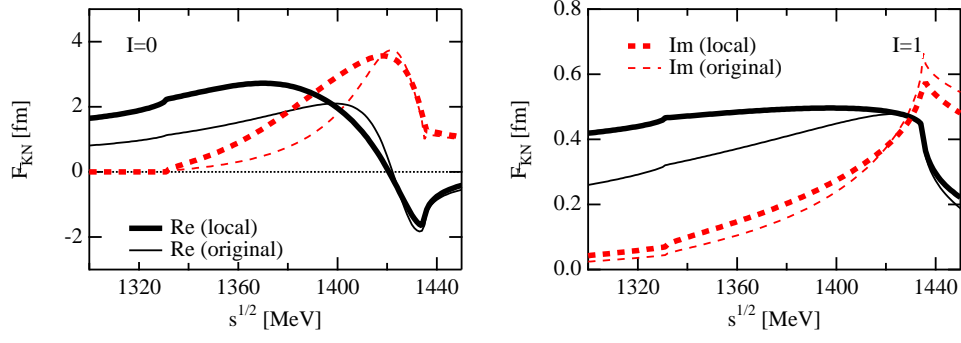


FIG. 10: (Color online) Scattering amplitudes $F_{\bar{K}N}$ from the local potential $U(r, E)$ (thick lines) and from the amplitude T^{eff} in the original chiral coupled-channel approach (thin lines) obtained by using the HNJH model for the $I = 0$ channel (left) and the $I = 1$ channel (right). Real parts are shown as solid lines and imaginary parts as dashed lines.

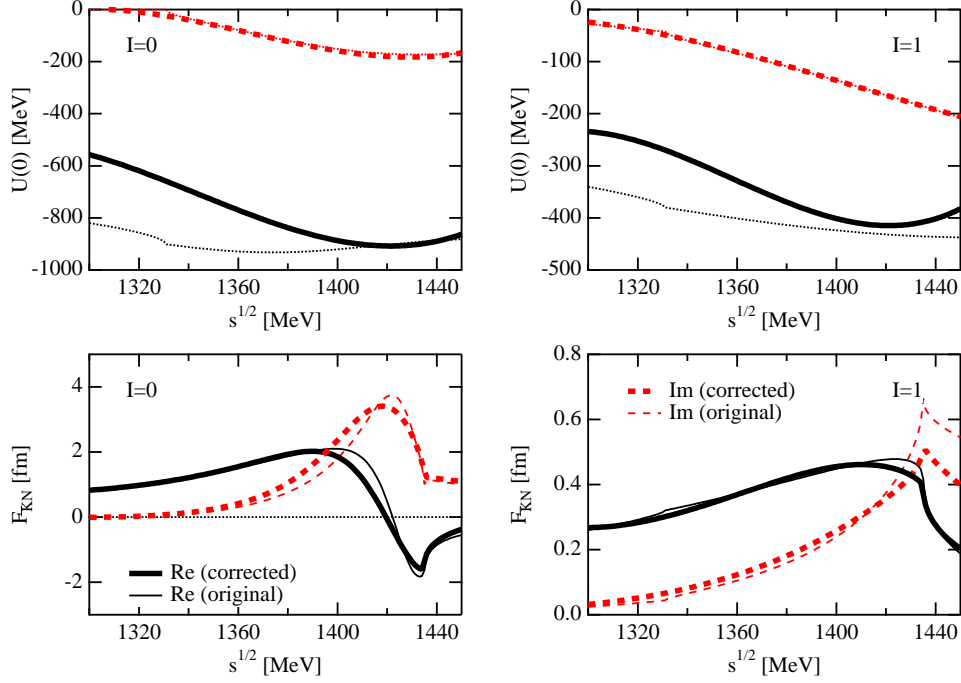


FIG. 11: (Color online) Upper panels: Strength of the fitted potential at $r = 0$ (thick lines) and the strength without correction [Eq. (11); dotted lines] with the HNJH model. Lower panels: Scattering amplitude f from the local potential (thick lines) and the amplitude T_{eff} in the original chiral unitary approach (thin lines) with the HNJH model. The real parts are shown by the solid lines and the imaginary parts are depicted by the dotted lines. Left: $I = 0$ channel. Right: $I = 1$ channel.

TABLE V: Coefficients of the polynomial of the effective interaction for $I = 0$.

Reference	K_0 (10^5 MeV)		K_1 (10^2 MeV^0)		K_2 (10^{-1} MeV^{-1})		K_3 (10^{-4} MeV^{-2})	
	Re	Im	Re	Im	Re	Im	Re	Im
ORB [35]	-3.9321	-4.5613	8.9088	10.097	- 6.709	- 7.4364	1.6771	1.8219
HNJH [34]	-5.1020	-4.3660	11.453	9.6378	- 8.5527	- 7.0773	2.1218	1.7285
BNW [29]	-4.3330	-6.6603	9.8635	14.710	- 7.4619	-10.812	1.8738	2.6443
BMN [33]	-6.6455	-4.0390	14.873	8.8408	-11.075	- 6.4345	2.7401	1.5568

TABLE VI: Coefficients of the polynomial of the effective interaction for $I = 1$.

Reference	K_0 (10^5MeV)		K_1 (10^2MeV^0)		K_2 (10^{-1}MeV^{-1})		K_3 (10^{-4}MeV^{-2})	
	Re	Im	Re	Im	Re	Im	Re	Im
ORB [35]	-6.2984	-0.63191	13.939	1.3709	-10.272	-0.98412	2.5195	0.23337
HNJH [34]	-4.4348	-0.67630	9.8340	1.4675	-7.2582	-1.0532	1.7818	0.24953
BNW [29]	-2.6295	-0.48818	5.8297	1.0484	-4.2999	-0.74387	1.0542	0.17396
BMN [33]	-7.5894	-0.52306	16.797	1.1074	-12.375	-0.77213	3.0330	0.17669

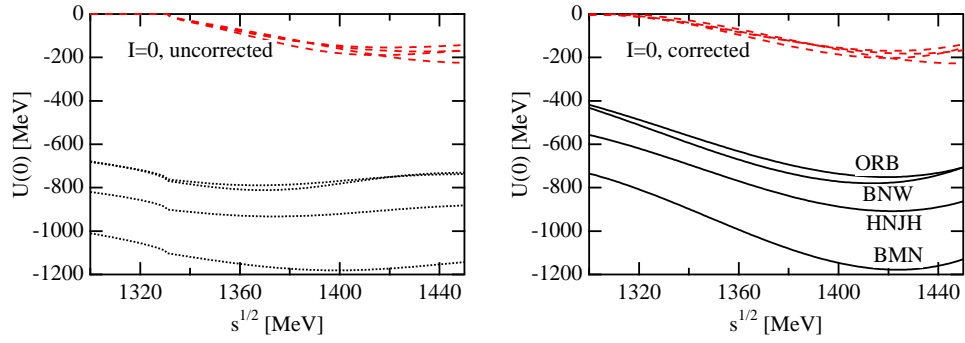


FIG. 12: (Color online) Strength of the local $I = 0$ $\bar{K}N$ potential $U(r, E)$ at $r = 0$ obtained by using different models as explained in the text. Left: Uncorrected potentials, with real parts shown as dotted lines. Right: Corrected potentials, with real parts shown as solid lines. Imaginary parts are depicted as dashed lines. The ordering of model assignments is the same in both panels.

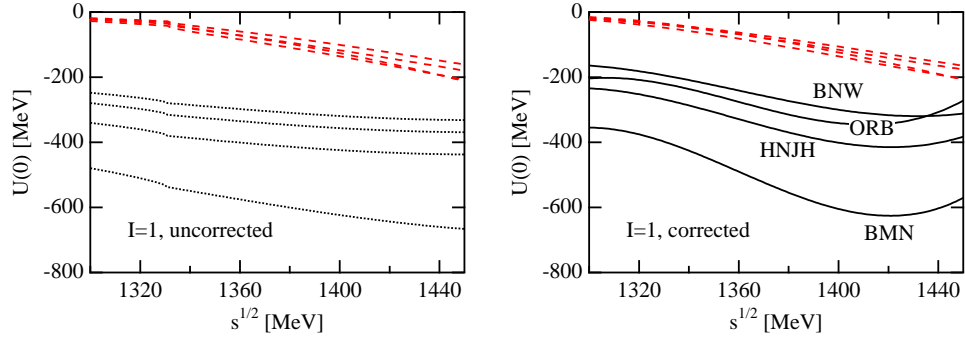


FIG. 13: (Color online) Strength of the local $I = 1$ $\bar{K}N$ potential $U(r, E)$ at $r = 0$ obtained by using different models as explained in the text. Left: Uncorrected potentials, with real parts shown as dotted lines. Right: Corrected potentials, with real parts shown as solid lines. Imaginary parts are depicted as dashed lines. The ordering of model assignments is the same in both panels.

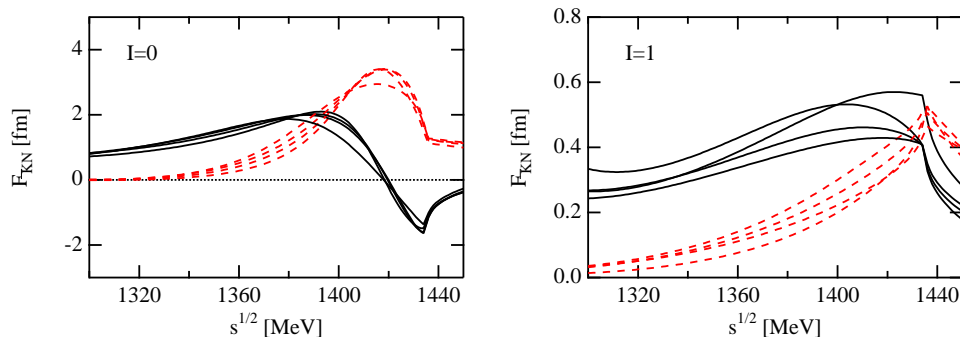


FIG. 14: (Color online) Scattering amplitudes $F_{\bar{K}N}$ from the corrected local potentials $U(r, E)$ for the four different models referred to in Figs. 12 and 13. Real parts are shown as solid lines and imaginary parts as dashed lines. Left: $I = 0$ channel. Right: $I = 1$ channel.

channels with $I = 0$, the AY potential reads

$$v_{ij}(r) = \begin{pmatrix} -436 & -412 \\ -412 & 0 \end{pmatrix} \exp[-(r/b)^2] \quad [\text{MeV}],$$

with $b \sim 0.66$ fm. Apart from the missing energy dependence, there are further qualitative differences between this potential and the interaction based on chiral SU(3) dynamics. The most drastic difference is the absence of a direct $\pi\Sigma \rightarrow \pi\Sigma$ coupling in the phenomenological potential. This is in sharp contrast with chiral dynamics, since the attractive interaction in the diagonal $\pi\Sigma$ channel is sufficiently strong to generate a resonance, as we have discussed in the previous sections. The coupled-channel dynamics leads to the quasibound structure in the $\bar{K}N$ system at around 1420 MeV.

The phenomenological AY model [21] starts from the “ansatz” that the $\Lambda(1405)$ resonance is a K^-p bound state. It shares this principal feature with chiral dynamics. However, the absence of the $\pi\Sigma \rightarrow \pi\Sigma$ coupling in the AY model has as its consequence that the $\Lambda(1405)$ is represented by only a single pole and the mass spectrum in the $\pi\Sigma$ channel is identical to that in the $\bar{K}N$ channel. This incorrectly implies a $\bar{K}N$ single-channel interaction that is too strongly attractive.

In Ref. [21], the equivalent single-channel potentials are given (in MeV) as

$$\begin{aligned} v_{\bar{K}N}^{I=0}(r) &= (-595 - i 83) \exp[-(r/0.66 \text{ fm})^2], \\ v_{\bar{K}N}^{I=1}(r) &= (-175 - i 105) \exp[-(r/0.66 \text{ fm})^2]. \end{aligned} \quad (12)$$

The amplitudes resulting from these potentials are shown in Fig. 15 by thin lines, to be compared with our present results (thick lines). The behavior of the amplitudes derived from the phenomenological potentials is seen to be drastically different from the chiral dynamics prediction, especially in the lower subthreshold energy region. The difference is certainly beyond the theoretical uncertainties estimated in Sec. III C. As we discussed, chiral dynamics locates the $\Lambda(1405)$ in the $\bar{K}N$ amplitude around 1420 MeV, whereas the phenomenological AY potential

uses the PDG value of around 1405 MeV. The difference is not only in the position of the $\Lambda(1405)$ but also in the magnitude of the amplitude. Note also that the imaginary parts remain finite even below the $\pi\Sigma$ threshold, since there is no energy dependence in the potentials (12).

However, above the $\bar{K}N$ threshold, both chiral and phenomenological amplitudes behave similarly as both approaches are adjusted to describe existing data. These and the previous observations clearly point out the considerable ambiguities involved in the extrapolation of the amplitudes below the $\bar{K}N$ threshold. Existing data sets are not sufficient to constrain the $\bar{K}N$ interaction in the energy region relevant for subthreshold antikaon-nucleon physics. At this point the minimal theoretical constraints from chiral SU(3) dynamics turn out to be of crucial importance.

V. SUMMARY

We have constructed an effective $\bar{K}N$ potential in coordinate space based on chiral SU(3) dynamics. This procedure involves two steps:

1. transforming the coupled-channel dynamics into a single channel $\bar{K}N$ interaction and
2. translating this effective interaction to an “equivalent” local potential.

Step 1 is exact within the chiral coupled-channels approach, whereas step 2 involves approximations.

In performing step 1 we have systematically investigated how the dynamics of the $\pi\Sigma$ channel (and of other channels, which turn out not to be important) influence the effective $\bar{K}N$ interaction. It is found that the $\pi\Sigma$ interaction generates a broad resonance whereas the $\bar{K}N$ interaction produces a weakly bound state. The attractive forces in the $\bar{K}N$ and $\pi\Sigma$ coupled channels cooperate to form the $\Lambda(1405)$ as a $\bar{K}N$ quasibound state embedded in the $\pi\Sigma$ continuum.

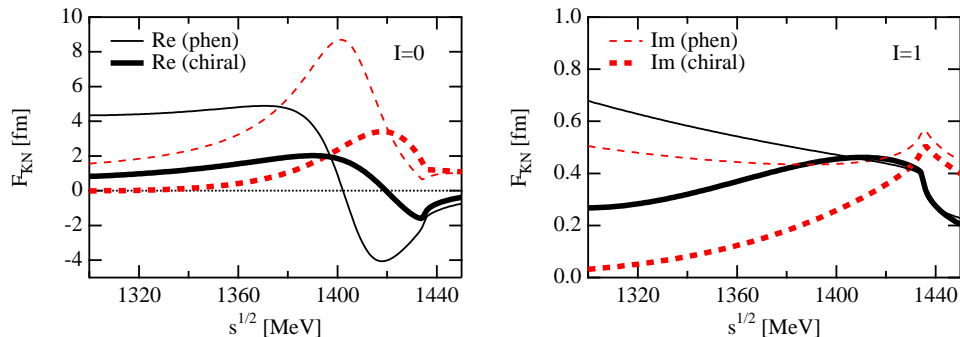


FIG. 15: (Color online) Comparison of the scattering amplitudes with phenomenological potential. Thick lines denote the results of the potentials derived in this work and thin lines denote the results of the phenomenological potential [21]. The real parts are shown by solid lines and the imaginary parts are depicted by dotted lines. Left: $I = 0$ channel. Right: $I = 1$ channel.

As a consequence of the two-pole structure of the coupled $\bar{K}N$ - $\pi\Sigma$ system, the $\bar{K}N$ quasibound state is located at $\sqrt{s} \simeq 1420$ MeV, at a mass shifted upward from the PDG value of $\Lambda(1405)$ deduced from the maximum of the $\pi\Sigma$ mass spectrum.

We have examined several versions of chiral SU(3) dynamical models to estimate theoretical uncertainties. The occurrence of the quasibound state at $\sqrt{s} \simeq 1420$ MeV turns out to be model independent, irrespective of the wide spread in the locations of the second pole. This implies that the $\bar{K}N$ binding energy associated with the $\Lambda(1405)$ is actually not 27 MeV but only 12 MeV, indicating significantly less attraction in the effective $\bar{K}N$ interaction than previously anticipated on purely phenomenological grounds.

In step 2, we have constructed an equivalent local potential, with a Gaussian r-space form factor reflecting finite range effects. The range parameter is adjusted so as to reproduce the position of the $\bar{K}N$ quasibound state and found to be somewhat smaller than that expected from a vector meson exchange picture. In any case, a local parametrization of the $\bar{K}N$ effective interaction works only with an adjustment of its energy dependence. This extra energy dependence considerably reduces the attractive strength of the potential in the subthreshold region as compared to naive expectations.

Uncertainties concerning subthreshold extrapolations of the effective $\bar{K}N$ interaction still remain as long as the constraints from threshold $\bar{K}N$ data and from the $\pi\Sigma$ mass spectrum in the $I = 0$ channel are relatively weak and partly ambiguous. There is a strong demand for fur-

ther improvements in this empirical data base. Nonetheless, the theoretical constraints on the strengths of the $\bar{K}N$ and $\pi\Sigma$ interactions from chiral SU(3) dynamics are certainly mandatory to reduce the freedom of extrapolation.

The potential so obtained suggests itself for applications in antikaon-nuclear few-body calculations. Results for the K^-pp prototype system are reported in Ref. [27]. The overall picture presented here, constrained by chiral SU(3) dynamics, differs strongly from previous purely phenomenological approaches, in that the resulting effective potential is significantly less attractive in the energy range relevant to the discussion of deeply bound antikaon-nuclear clusters.

Acknowledgments

The authors thank Avraham Gal and Akinobu Doté for many helpful discussions. This project is partially supported by BMBF, GSI, and by the DFG excellence cluster “Origin and Structure of the Universe.” T. H. thanks the Japan Society for the Promotion of Science (JSPS) for financial support. His work is supported in part by the Grant for Scientific Research (No. 19853500) from the Ministry of Education, Culture, Sports, Science and Technology (MEXT) of Japan. This research is part of the Yukawa International Program for Quark-Hadron Science.

-
- [1] T. Suzuki *et al.*, Phys. Lett. **B597**, 263 (2004).
 - [2] M. Sato *et al.*, Phys. Lett. **B659**, 107 (2008).
 - [3] M. Agnello *et al.*, (FINUDA collaboration), Phys. Rev. Lett. **94**, 212303 (2005).
 - [4] E. Oset and H. Toki, Phys. Rev. C **74**, 015207 (2006).
 - [5] V. K. Magas, E. Oset, A. Ramos, and H. Toki, Phys.

- Rev. C **74**, 025206 (2006).
- [6] G. E. Brown, C. H. Lee, M. Rho, and V. Thorsson, Nucl. Phys. **A567**, 937 (1994).
- [7] T. Waas, N. Kaiser, and W. Weise, Phys. Lett. **B379**, 34 (1996).
- [8] T. Waas and W. Weise, Nucl. Phys. **A625**, 287 (1997).

- [9] T. Waas, M. Rho, and W. Weise, Nucl. Phys. **A617**, 449 (1997).
- [10] M. F. M. Lutz and C. L. Korpa, Nucl. Phys. **A700**, 309 (2002).
- [11] M. F. M. Lutz, C. L. Korpa, and M. Moller, arXiv:0707.1283 [nucl-th].
- [12] D. B. Kaplan and A. E. Nelson, Phys. Lett. **B175**, 57 (1986).
- [13] D. B. Kaplan and A. E. Nelson, Nucl. Phys. **A479**, 273 (1988).
- [14] Y. Akaishi and T. Yamazaki, Phys. Rev. C **65**, 044005 (2002).
- [15] A. Dote, H. Horiuchi, Y. Akaishi, and T. Yamazaki, Phys. Rev. C **70**, 044313 (2004).
- [16] A. Dote, Y. Akaishi, and T. Yamazaki, Prog. Theor. Phys. Suppl. **156**, 184 (2004).
- [17] W. Weise, nucl-th/0701035.
- [18] N. V. Shevchenko, A. Gal, and J. Mares, Phys. Rev. Lett. **98**, 082301 (2007).
- [19] N. V. Shevchenko, A. Gal, J. Mares, and J. Revai, Phys. Rev. C **76**, 044004 (2007).
- [20] Y. Ikeda and T. Sato, Phys. Rev. C **76**, 035203 (2007).
- [21] T. Yamazaki and Y. Akaishi, Phys. Rev. C **76**, 045201 (2007).
- [22] N. Kaiser, P. B. Siegel, and W. Weise, Nucl. Phys. **A594**, 325 (1995).
- [23] E. Oset and A. Ramos, Nucl. Phys. **A635**, 99 (1998).
- [24] J. A. Oller and U. G. Meissner, Phys. Lett. **B500**, 263 (2001).
- [25] M. F. M. Lutz and E. E. Kolomeitsev, Nucl. Phys. **A700**, 193 (2002).
- [26] A. Dote and W. Weise, Prog. Theor. Phys. Suppl. **168**, 593 (2007).
- [27] A. Dote, T. Hyodo, and W. Weise, arXiv:0802.0238 [nucl-th].
- [28] B. Borasoy, R. Nissler, and W. Weise, Phys. Rev. Lett. **94**, 213401 (2005).
- [29] B. Borasoy, R. Nissler, and W. Weise, Eur. Phys. J. A **25**, 79 (2005).
- [30] T. Hyodo, S. I. Nam, D. Jido, and A. Hosaka, Prog. Theor. Phys. **112**, 73 (2004).
- [31] J. A. Oller, J. Prades, and M. Verbeni, Phys. Rev. Lett. **95**, 172502 (2005).
- [32] J. A. Oller, Eur. Phys. J. A **28**, 63 (2006).
- [33] B. Borasoy, U. G. Meissner, and R. Nissler, Phys. Rev. C **74**, 055201 (2006).
- [34] T. Hyodo, S. I. Nam, D. Jido, and A. Hosaka, Phys. Rev. C **68**, 018201 (2003).
- [35] E. Oset, A. Ramos, and C. Bennhold, Phys. Lett. **B527**, 99 (2002).
- [36] D. Jido, J. A. Oller, E. Oset, A. Ramos, and U. G. Meissner, Nucl. Phys. **A725**, 181 (2003).
- [37] T. Hyodo, A. Hosaka, E. Oset, A. Ramos, and M. J. Vicente Vacas, Phys. Rev. C **68**, 065203 (2003).
- [38] V. K. Magas, E. Oset, and A. Ramos, Phys. Rev. Lett. **95**, 052301 (2005).
- [39] C. Garcia-Recio, M. F. M. Lutz, and J. Nieves, Phys. Lett. **B582**, 49 (2004).
- [40] R. J. Hemingway, Nucl. Phys. **B253**, 742 (1985).
- [41] D. W. Thomas, A. Engler, H. E. Fisk, and R. W. Kraemer, Nucl. Phys. **B56**, 15 (1973).
- [42] LEPS, J. K. Ahn, Nucl. Phys. **A721**, 715 (2003).
- [43] S. Prakhov *et al.*, (Crystall Ball Collaboration), Phys. Rev. C **70**, 034605 (2004).
- [44] I. Zychor *et al.*, Phys. Lett. **B660**, 167 (2008).
- [45] Particle Data Group, W. M. Yao *et al.*, J. Phys. G **33**, 1 (2006).
- [46] R. H. Dalitz and A. Deloff, J. Phys. G **17**, 289 (1991).
- [47] J. C. Nacher, E. Oset, H. Toki, and A. Ramos, Phys. Lett. **B455**, 55 (1999).
- [48] T. Hyodo, A. Hosaka, M. J. Vicente Vacas, and E. Oset, Phys. Lett. **B593**, 75 (2004).
- [49] N. Kaiser, T. Waas, and W. Weise, Nucl. Phys. **A612**, 297 (1997).
- [50] A. D. Martin, Nucl. Phys. **B179**, 33 (1981).
- [51] One can equivalently use the same formulation for the standard integral equation, regarding the channel indices as intermediate momenta.
- [52] In our present calculations, the isospin averaged \bar{K} mass has been used in practice, so that the $\bar{K}N$ threshold actually appears at $\sqrt{s} = 1435$ MeV, shifted by 3 MeV from the K^-p threshold. The value of the binding energies just mentioned are thus understood to be shifted by the same amount.
- [53] For the ORB model, it was stated that $f = 1.15 \times f_\pi$ in Ref. [35], but in the actual calculation $f = 1.123 \times f_\pi$ was used, as noted in Ref. [36]. For the BNW model, there is a misprint in the column “WT term” in Table 1 of Ref. [29]: The signs of all subtraction constants should be inverted.
- [54] In practice, $\pi^0 \Sigma^0$ has no $I = 1$ component and the contribution from $I = 2$ is considered to be small.